Nanoscale

Accepted Manuscript

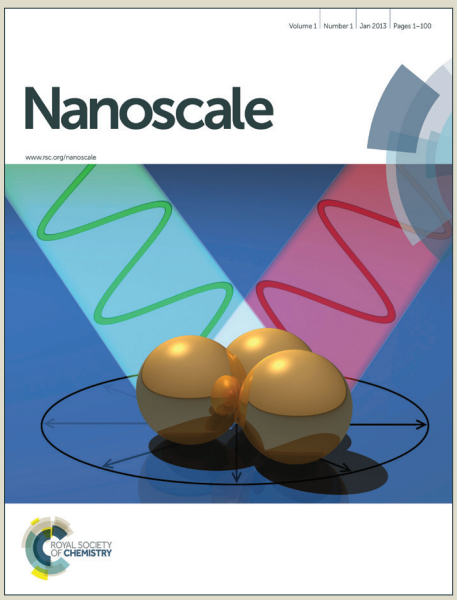

ROYAL SOCIETY OF CHEMISTRY

www.rsc.org/nanoscale

ARTICLE TYPE www. rsc.org/xxxxxx | XXXXXXXX

Probing Charge Transfer Excitons in a $MoSe_2$-WS_2 van der Waals Heterostructure

Frank Ceballos,[a] Matthew Z. Bellus,[a] Hsin-Ying Chiu,[a] and Hui Zhao*[a]

Received Xth XXXXXXXXXX 20XX, Accepted Xth XXXXXXXXX 20XX
First published on the web Xth XXXXXXXXXX 200X
DOI: 10.1039/b000000x

We show that the van der Waals heterostructure formed by $MoSe_2$ and WS_2 provides a unique system with near degenerate interlayer and intralayer excitonic states. Photoluminescence measurements indicate that the charge transfer exciton states are approximately 50 meV below the $MoSe_2$ exciton states, with a significant spectral overlap. The transient absorption of a femtosecond pulse was used to study the dynamics of the charge transfer excitons at room temperature. We found a lifetime of approximately 80 ps for the charge transfer excitons. A diffusion coefficient of about 14 cm^2 s^{-1} was deduced, which is comparable to individual excitons in transition metal dichalcogenides.

1 Introduction

Layered materials represent a diverse and largely unexplored source of two-dimensional materials with exotic properties that can be very different from their bulk counterparts[1]. Among them, transition metal dichalcogenides (TMDs) have drawn considerable attention since 2010[2]. They have several exotic properties such as an indirect to direct band gap transition in monolayers[3,4], valley-selective optical coupling[5–7], and large binding energies of excitons, trions, and biexcitons[8–10]. In addition to their potential applications as individual materials in field-effect transistors[11], solar cells[12,13], light-emitting diodes[14], and sensors[15], these atomic layers are being used as the building blocks for new van der Waals heterostructures[16]. These heterostructures can potentially combine the novel properties of TMDs for targeted applications.

Six different types of bilayer heterostructures can be formed by utilizing MoS_2, $MoSe_2$, WS_2, and WSe_2, the four most extensively studied TMDs. The following five combinations have been fabricated and studied: MoS_2-$MoSe_2$[17], MoS_2-WS_2[18–22], MoS_2-WSe_2[23–29], $MoSe_2$-WSe_2[30], and WS_2-WSe_2[31]. These heterostructures have qualitatively similar properties and as predicted by first-principles calculations[32,33] their band alignment is of type-II, where the bottom of the conduction and the top of the valence bands reside in different layers. Hence, electrons and holes, once excited in either layer, are incline to spatially separate to the two layers and form charge transfer excitons, as observed from photoluminescence (PL) quenching[19,21,23,24] and time resolved measurements[17,18]. Due to the large offsets (in energy) between the conduction band minimum in one layer and the valence band maximum in the other layer, the energy states of the charge transfer excitons are far away from the direct exciton states. The increase in spatial separation of the electron and hole wave functions results in long lived charge transfer excitons[30].

Here we show that the less studied heterostructure, $MoSe_2$-WS_2, is in fact the only one that has near degenerate direct exciton and charge transfer exciton states. PL measurements showed that the charge transfer exciton states are only 50 meV below the $MoSe_2$ excitons, with significant overlap of the two PL peaks. Temporally and spatially resolved measurements revealed that the transport properties of the charge transfer excitons are similar to that of direct excitons in TMD monolayers. The near degenerate exciton states indicate the small conduction band offset in $MoSe_2$-WS_2 heterostructure, which facilitates gate control of charge transfer.

2 Experimental Section

To fabricate the heterostructure sample, we first obtained monolayer flakes of $MoSe_2$ and WS_2 on polydimethylsiloxane (PDMS) substrates, following the standard procedures of mechanical exfoliation. The $MoSe_2$ flake was then transfer to a Si substrate with a 90 nm SiO_2 layer. The sample was then cleaned in acetone, rinsed with isopropanol, dried under nitrogen, and annealed for 2 h at 200°C in a H_2/Ar (10 sccm/100 sccm) environment with a pressure of 3 Torr. Next, the WS_2 flake is transfer onto the $MoSe_2$ flake, followed by the same cleaning and annealing procedure.

The PL system is based on a Horiba iHR550 imaging spectrometer equipped with a thermoelectrically cooled charge-coupled device (CCD) camera. A diode laser beam of 405-nm

[a] *Department of Physics and Astronomy, The University of Kansas, Lawrence, Kansas 66045, USA. Fax: 1 785 864 5262; Tel: 1 785 864 1938; E-mail: huizhao@ku.edu.*

is focused to the sample through a microscope objective lens. An imaging system was used to observe and locate the laser spot on the flake. The PL was collected by the same objective lens and then guided to the spectrometer.

The differential reflection setup utilizes a laser system composed of a Ti-sapphire laser with a repetition rate of 81 MHz and an optical parametric oscillator. The pulses of 790 and 810 nm were obtained from the Ti-sapphire laser directly, while second-harmonic generation of this output in a beta barium borate crystal was used to obtain the pulses of 385 and 395 nm. The 730 nm pulse was obtained by second harmonic generation of the output of the optical parametric oscillator. To obtain the 620 nm pulse, supercontinnum generation from the Ti:sapphire output in a photonic crystal fiber was utilized, with a bandpass filter to select the desired spectral component. All the pulses are shorter than 300 fs. In each pump/probe configuration, the two pulses were focused to the sample from normal direction by a microscope objective lens. The reflected probe pulse was sent to a silicon photodetector, which output was measured by a lock-in amplifier. The pump pulse was modulated by a mechanical chopper at about 2 KHz.

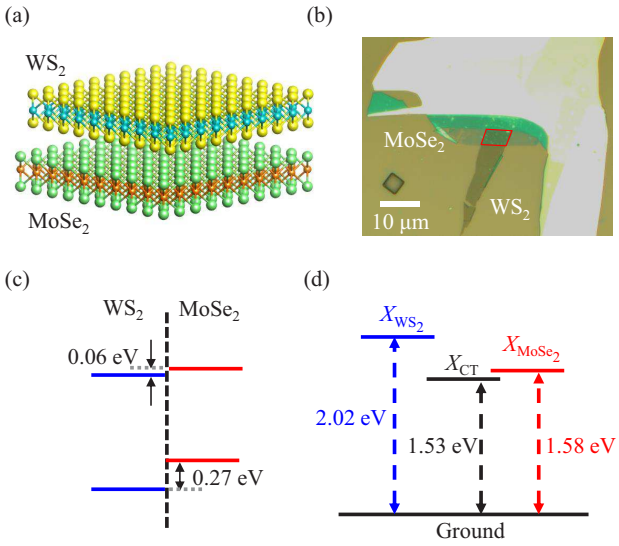

Fig. 1 (a) Schematic illustration of the $MoSe_2$-WS_2 heterostructure sample. (b) Microscope images of sample containing the heterostructure (indicated by the red box) and individual $MoSe_2$ and WS_2 monolayer regions on a Si-SiO_2 substrate. (c) Band alignment predicted by first principles calculations[33], showing 60 and 270 meV conduction and valence band offsets, respectively. (d) Energy diagram of exciton states determined by the photoluminescence spectrum.

3 Results and Discussion

3.1 Excitonic States in $MoSe_2$-WS_2 Heterostructure

The WS_2-$MoSe_2$ heterostructure sample studied is shown schematically in Figure 1a (and visually Figure 1b). The monolayers composing the heterostructure have neighboring secluded regions of WS_2 and $MoSe_2$ which ease the comparison between any measurement done in the heterostructure and its constituent monolayers. No efforts were made to determine and control the relative orientations of the two flakes; as a matter of fact, the WS_2 location was selected so that the heterostructure region contained a large area. In all the measurements reported in this paper, the sample was kept under an ambient condition. No sample degradation was observed during the course of the entire study.

Recently, two groups have predicted, using first-principle calculations[32,33], that the conduction band offset of $MoSe_2$ and WS_2 could be as small as 20 or 60 meV. Figure 1c shows schematically the type-II band alignment of this heterostructure, where the near degenerate conduction bands facilitate control of electron population between the two layers which can be utilized in tunneling-based devices.

We begin our study by conducting PL spectroscopy on the heterostructure and its neighboring monolayers. To generate the PL a continuous wave laser with a 405 nm wavelength and incident power of 0.6 μW was focused onto a perpendicular placed sample using a $\times 50$ microscope objective lens. The PL spectra of the WS_2 (blue), $MoSe_2$ (red), and WS_2-$MoSe_2$ heterostructure (black), shown in Figure 2, were collected by an imaging spectrometer equipped with a thermoelectrically cooled CCD camera. An intense PL emission centered at 617.3 nm was observed when the laser spot was located on the WS_2 monolayer region (blue curve in Figure 2, divided by 23). The peak position, linewidth, and PL yield are all reasonably consistent with previous reports[34–38], further confirming its monolayer thickness. When the laser spot was placed on the $MoSe_2$ region, a much weak PL peak was observed at 785.5 nm (red curve in Figure 2), which is also consistent with previous results[39–41].

Of more interest is the heterostructure PL spectrum which exhibits two peaks at 614.7 nm and 810.0 nm. Without interlayer coupling or charge transfer, the PL spectrum of the heterostructure is expected to be the sum of the two monolayer individual spectra. However, the 614.7 nm peak, due to the radiative recombination of excitons in the WS_2 layer of the heterostructure, is close to the WS_2 monolayer peak but it is slightly blue shifted due to the different dielectric environment present in the heterostructure. Moreover, its magnitude has been quenched by a factor of 23, suggesting that most of the holes created in WS_2 transferred to $MoSe_2$ before forming direct excitons and recombining radiatively. A similar PL quenching effect has been recently observed on WS_2-MoS_2 heterostructures with clean interfaces[18–22]. In addition, its shape displays a shoulder, absent in the WS_2 PL spectrum,

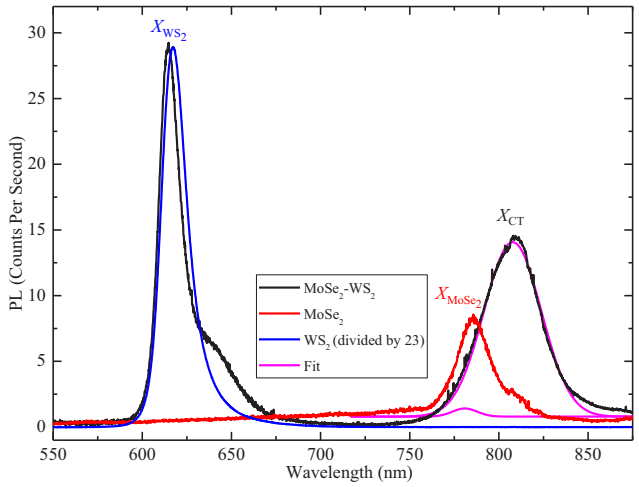

Fig. 2 Room-temperature photoluminescence spectra of the $MoSe_2$-WS_2 heterostructure (black) and individual WS_2 (blue, divided by 23) and $MoSe_2$ (red) monolayers obtained under the same condition. The pink curves are the two components of a double-Gaussian fit to the 810 nm peak.

that occurs at longer wavelengths from the 614.7 nm peak and is attributed to the formation of trions [42].

The strong peak at 810.0 nm, observed in the heterostructure, appears near the spectral range of the $MoSe_2$ exciton. The following facts show that the excitons in $MoSe_2$ are not the origin of it. First, the 810.0 nm peak in the heterostructrue is shifted 25.0 nm to the longer wavelength of the $MoSe_2$ monolayer PL peak (785.5 nm). When forming heterostructures, the exciton binding energies are expected to slightly change due to the different dielectric environment; actually, previous measurements show that the shift of the $MoSe_2$ PL peak is at most a few nanometers when forming heterostructures with MoS_2 [17] and WSe_2 [30]. Considering the similar dielectric properties of these TMDs, it is unlikely that WS_2 would cause a 25 nm shift of the $MoSe_2$ exciton peak. In fact, in this sample, the shift of the WS_2 peak is only 2.6 nm. Second, previous studies on TMD heterostructures have all observed PL quenching. Specifically, exciton PL of $MoSe_2$ was found to be reduced by a factor of 15 when forming a heterostructure with MoS_2 [17] and by a factor of 5 with WSe_2 [30]. However, the 810 nm peak magnitude in our $MoSe_2$-WS_2 heterostructure sample is twice as large than the magnitude of the $MoSe_2$ monolayer, strongly suggesting that it is not from excitons in $MoSe_2$. Furthermore, by fitting the 810 nm peak with two Gaussian functions (pink curves), we were able to identify a small component that is about 10 times lower than the $MoSe_2$ exciton peak. This is likely the quenched $MoSe_2$ peak in the heterostructure.

Having excluded the $MoSe_2$ excitons as the origin, we attribute the 810 nm peak to the spatially indirect excitons, known as charge transfer excitons (X_{CT}). Upon optical excitation of a 405.0 nm laser, electron and holes are injected into two both layers. This would normally produce direct excitons that would reside and decay in the particular layer they were produced; however, as a result of the HT type-II band alignment, where the minimum of the conduction band is located in the WS_2 monolayer and the maximum of the valence band is in the $MoSe_2$ monolayer, spatial separation of most electrons and holes after photoexcitation will ensue. Despite the fact that electrons populate the WS_2 and holes the $MoSe_2$ monolayers, their electrostatic Coulomb force bounds them together to form charge transfer excitons. With this assignment, we can construct the exciton energy states diagram as shown in Figure 1d. The energy difference of 50 meV between the charge transfer and $MoSe_2$ excitons is order-of-magnitude consistent with the theoretical predictions on the conduction band offset [32,33].

We note that the annealing process described in Sec. 2 is necessary for forming a clean interface between the two monolayers, which is required for efficient charge transfer. Samples before the annealing process show no sign of charge transfer, with PL spectra similar to the sum of the spectra of individual monolayers.

3.2 Probing the Charge Transfer Excitons

To further confirm the observation of the charge transfer excitons, we performed transient absorption measurements in reflection geometry. A 730 nm pump pulse with a peak fluence of 5.6 μJ cm^{-2} is used to inject excitons in the $MoSe_2$ layer of the heterostructure sample. To monitor the charge transfer excitons, we measured the differential reflection of a 810 nm probe pulsed (tuned to the charge transfer exciton PL peak) . The differential reflection is defined as the relative changed of the probe reflection cause by the presence of the pump. Symbolically, this is noted as $\Delta R/R_0 = (R - R_0)/R_0$, where R and R_0 are the probe reflection with and without the presence of the pump, respectively. We observed a strong differential reflection signal with a magnitude on the order of 10^{-3}, as shown as the black curves in Figure 3, that reaches a peak immediately following the pump excitation. The ultrafast rise of the signal is a clear indication that charge transfer excitons are formed in an ultrashort time scale.

Two control experiments were performed to ensure that the charge transfer excitons were probed. First, we repeated the measurement on the $MoSe_2$ monolayer region of the flake, where no signal could be measured (shown as the blue curves on Figure 3) since the 810 nm pulse is well below the exciton resonance of $MoSe_2$. Second, we used the 810-nm pulse as the pump and 730-nm pulse as the probe on the heterostructure sample. No signal was observed (shown as the purple

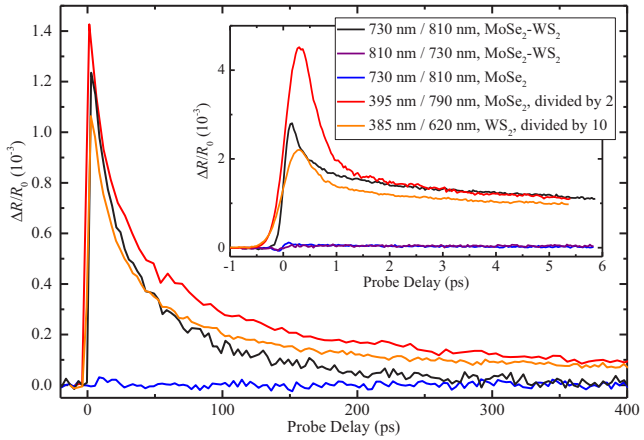

Fig. 3 Differential reflection signals measured with 730 nm pump and 810 nm probe pulses from the $MoSe_2$-WS_2 heterostructure (black) and individual $MoSe_2$ (blue) at room temperature. The red and orange curves are signals from individual $MoSe_2$ and WS_2 monolayers, with 395 nm/790 nm and 385 nm/620 nm pump/probe wavelengths, respectively. The purple curve shows the signal from the heterostructure sample with 810 nm/730 nm configuration. The inset shows the results near zero probe delay.

curve on Figure 3), which further confirms the nature of the 810-nm peak. As a spatially indirect transition, its absorption is expected to be weak and even if some charge transfer excitons are injected by the 810-nm pump, they cannot populate the $MoSe_2$ exciton states; therefore, they should not be detected by the 730-nm probe. These two measurements prove unambiguously that the black curves shown in Figure 3 are indeed from the charge transfer excitons.

To compare the charge transfer excitons with excitons in the individual monolayers, we probed the excitons in $MoSe_2$ (395 nm pump and 790 nm probe, red curve) and WS_2 (385 nm pump and 620 nm probe, orange curve) regions. We found that under the same conditions, the differential reflection signals when probing the monolayers were larger than the signal of the charge transfer excitons. Although part of the difference could be attributed to changes of absorption coefficient at different pump wavelengths, the indirect nature of the charge transfer exciton absorption should result in a weaker transient absorption response.

3.3 Dynamics of Charge Transfer Excitons

Having established the probe of charge transfer excitons, we used the 730 nm pump and 810 nm probe to study the dynamics of charge transfer excitons.

First, to study the recombination of charge transfer excitons, we performed time-resolved differential reflection measurements with different values of the pump fluence. Figure

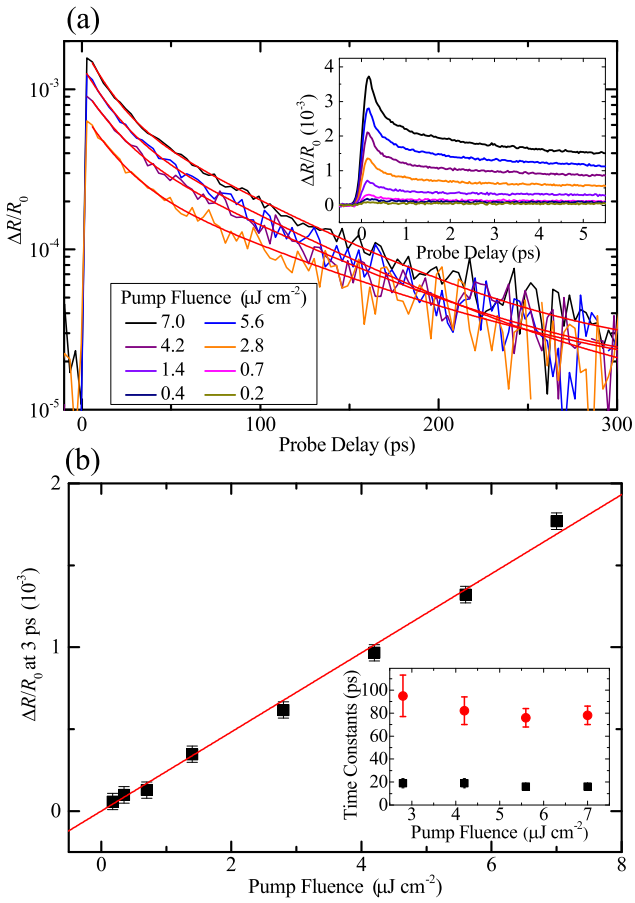

Fig. 4 (a) Differential reflection signals measured at room temperature with 730 nm pump and 810 nm probe pulses from the $MoSe_2$-WS_2 heterostructure with different values of the pump pulse fluence as indicated. The red curves are biexponential fits. (b) The magnitude of the differential reflection signal, represented by the signal at a probe delay of 3 ps, as a function of the pump fluence. The inset shows the short (black squares) and long (red circles) time constants obtained from the fits shown in (a).

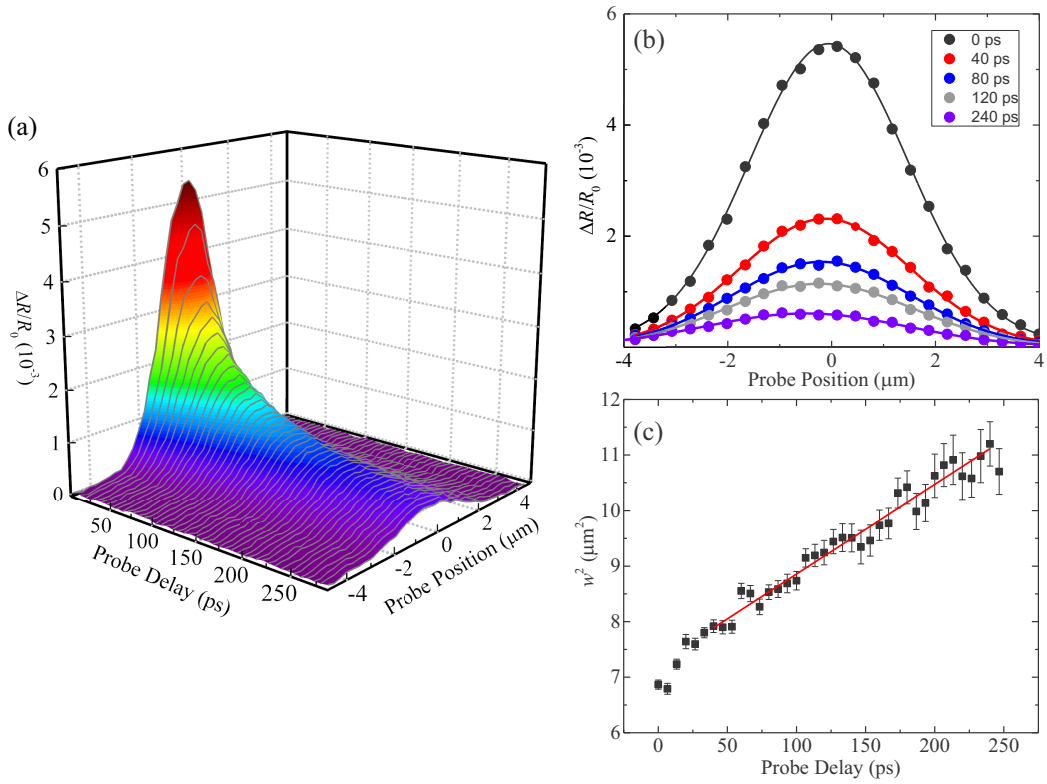

Fig. 5 (a) Differential reflection signal of the $MoSe_2$-WS_2 heterostructure as a function of the probe delay and probe position at room temperature. The pump and probe wavelengths are 730 and 810 nm, respectively. (b) Examples of the spatial profiles of differential reflection at several probe delays. The solid curves are Gaussian fits. (c) Squared width of the profile deduced from Gaussian fits as a function of the probe delay. The linear fit, as indicated by the red line, corresponds to an exciton diffusion coefficient of 14 cm^2 s^{-1}.

4a shows the decay of the signal, with the pump fluences indicated in the figure. We find that the magnitude of the signal is proportional to the pump fluence, as summarized in Figure 4b, which shows that the transient absorption signal is proportional to the density of the charge transfer excitons. After a short transient of less than 1 ps, the rest of the decay can be well described by bi-exponential functions, as confirmed by the fits shown as the red curves in Figure 4a. The two time constants obtained from these fits are summarized in the inset of Figure 4b. We found that in this range, the decay constants are independent of the pump fluence, which shows the multiexciton recombination process play an unimportant role in the dynamics of charge transfer excitons. This is in contrast to exciton dynamics in monolayer $MoSe_2$, where a density-dependent dynamics due to exciton-exciton annihilation was observed[40]. We attribute the long time constant of approximately 80 ps to the lifetime of charge transfer excitons. Given the expected long radiative lifetime of these excitons, the lifetime deduce here is likely limited by nonradiative recombination. The short time constant of less than 20 ps can be attributed to energy relaxation since the carriers are injected with large excess energies.

Next, we performed spatially resolved differential reflection measurements to study the diffusion of charge transfer excitons. Here, the pump and probe pulses are both focused to about 2 μm in full width at half maximum. The distance between the centers of the pump and probe spots, defined as the probe position (with respect to the pump spot center), can be adjusted by slightly changing the incident angle of the beam to the objective lens. By measuring the differential reflection signal as a function of the probe delay at each probe position, we obtain the evolution of the signal as a function of both time and space, as plotted in Figure 5a. At each probe delay, the spatial profile has a Gaussian shape. Figure 5b shows a few examples of these profiles, along with the Gaussian fits (solid curves). The squared width deduced from all the fits are plotted in Figure 5c, as a function of the probe delay.

In this process, the pump pulse injects excitons in $MoSe_2$, which form charge transfer excitons rapidly after the electrons moved to WS_2 that then diffuse in the heterostructure, driven by the in-plane density gradient. This diffusion process can be described by the classic diffusion equation, which predicts that the squared width of the profile increases linearly as $w^2(t) = w_0^2 + 4Dt$, where D and w_0 are the exciton diffusion coefficient and the initial width, respectively[43]. We find that this model can well describe the expansion of the profile after about 20 ps. By a linear fit, as indicated by the red line in Figure 5c, we obtain a diffusion coefficient of 14 ± 3 cm^2 s^{-1}. This value is similar to exciton diffusion coefficient in individual TMD monolayers[44,45], showing that the spatial indirect nature of the charge transfer excitons does not significantly change its in-plane transport property.

4 Conclusions

We present multiple evidences that the 810 nm PL peak originates from charge transfer excitons in the $MoSe_2$-WS_2 heterostructures. Based on that, we constructed the energy diagram of excitons states of this structure, with near degenerate charge transfer and $MoSe_2$ exciton states. Our PL measurement confirmed the theoretical predictions of the small conduction band offset of this structure. Finally, through transient absorption measurements with high temporal and spatial resolution, we obtained a lifetime of 80 ps and an in-plane diffusion coefficient of 14 cm^2 s^{-1} for these charge transfer excitons.

5 Acknowledgements

This material is based upon work supported by the National Science Foundation of USA under Award Nos. DMR-0954486 and IIA-1430493.

References

1 K. S. Novoselov, A. K. Geim, S. V. Morozov, D. Jiang, Y. Zhang, S. V. Dubonos, I. V. Grigorieva and A. A. Firsov, *Science*, 2004, **306**, 666–669.
2 Q. H. Wang, K. Kalantar-Zadeh, A. Kis, J. N. Coleman and M. S. Strano, *Nat. Nanotechnol.*, 2012, **7**, 699–712.
3 K. F. Mak, C. Lee, J. Hone, J. Shan and T. F. Heinz, *Phys. Rev. Lett.*, 2010, **105**, 136805.
4 A. Splendiani, L. Sun, Y. Zhang, T. Li, J. Kim, C. Y. Chim, G. Galli and F. Wang, *Nano Lett.*, 2010, **10**, 1271–1275.
5 D. Xiao, G. B. Liu, W. Feng, X. Xu and W. Yao, *Phys. Rev. Lett.*, 2012, **108**, 196802.
6 H. Zeng, J. Dai, W. Yao, D. Xiao and X. Cui, *Nat. Nanotechnol.*, 2012, **7**, 490–493.
7 K. F. Mak, K. He, J. Shan and T. F. Heinz, *Nat. Nanotechnol.*, 2012, **7**, 494–498.
8 K. F. Mak, K. He, C. Lee, G. H. Lee, J. Hone, T. F. Heinz and J. Shan, *Nat. Mater.*, 2013, **12**, 207–211.
9 A. Chernikov, T. C. Berkelbach, H. M. Hill, A. Rigosi, Y. L. Li, O. B. Aslan, D. R. Reichman, M. S. Hybertsen and T. F. Heinz, *Phys. Rev. Lett.*, 2014, **113**, 076802.
10 K. He, N. Kumar, L. Zhao, Z. Wang, K. F. Mak, H. Zhao and J. Shan, *Phys. Rev. Lett.*, 2014, **113**, 026803.
11 B. Radisavljevic, A. Radenovic, J. Brivio, V. Giacometti and A. Kis, *Nat. Nanotechnol.*, 2011, **6**, 147–150.
12 A. Pospischil, M. M. Furchi and T. Mueller, *Nat. Nanotechnol.*, 2014, **9**, 257–261.
13 B. W. H. Baugher, H. O. H. Churchill, Y. Yang and P. Jarillo-Herrero, *Nat. Nanotechnol.*, 2014, **9**, 262–267.
14 Y. J. Zhang, T. Oka, R. Suzuki, J. T. Ye and Y. Iwasa, *Science*, 2014, **344**, 725–728.
15 D. Sarkar, W. Liu, X. Xie, A. C. Anselmo, S. Mitragotri and K. Banerjee, *ACS Nano*, 2014, **8**, 3992–4003.
16 A. K. Geim and I. V. Grigorieva, *Nature*, 2013, **499**, 419–425.
17 F. Ceballos, M. Z. Bellus, H. Y. Chiu and H. Zhao, *ACS Nano*, 2014, **8**, 12717–12724.
18 X. Hong, J. Kim, S. F. Shi, Y. Zhang, C. Jin, Y. Sun, S. Tongay, J. Wu, Y. Zhang and F. Wang, *Nat. Nanotechnol.*, 2014, **9**, 682–686.

19 Y. Gong, J. Lin, X. Wang, G. Shi, S. Lei, Z. Lin, X. Zou, G. Ye, R. Vajtai, B. I. Yakobson, H. Terrones, M. Terrones, B. K. Tay, J. Lou, S. T. Pantelides, Z. Liu, W. Zhou and P. M. Ajayan, *Nat. Mater.*, 2014, **13**, 1135–1142.

20 Y. F. Yu, S. Hu, L. Q. Su, L. J. Huang, Y. Liu, Z. H. Jin, A. A. Purezky, D. B. Geohegan, K. W. Kim, Y. Zhang and L. Y. Cao, *Nano Lett.*, 2015, **15**, 486–491.

21 S. Tongay, W. Fan, J. Kang, J. Park, U. Koldemir, J. Suh, D. S. Narang, K. Liu, J. Ji, J. Li, R. Sinclair and J. Wu, *Nano Lett.*, 2014, **14**, 3185–3190.

22 J. T. Yuan, S. Najmaei, Z. H. Zhang, J. Zhang, S. D. Lei, P. M. Ajayan, B. I. Yakobson and J. Lou, *ACS Nano*, 2015, **9**, 555–563.

23 H. Fang, C. Battaglia, C. Carraro, S. Nemsak, B. Ozdol, J. S. Kang, H. A. Bechtel, S. B. Desai, F. Kronast, A. A. Unal, G. Conti, C. Conlon, G. K. Palsson, M. C. Martin, A. M. Minor, C. S. Fadley, E. Yablonovitch, R. Maboudian and A. Javey, *Proc. Natl. Acad. Sci. U. S. A.*, 2014, **111**, 6198–6202.

24 M. H. Chiu, M. Y. Li, W. Zhang, W. T. Hsu, W. H. Chang, M. Terrones, H. Terrones and L. J. Li, *ACS Nano*, 2014, **8**, 9649–9656.

25 T. Roy, M. Tosun, X. Cao, H. Fang, D. H. Lien, P. D. Zhao, Y. Z. Chen, Y. L. Chueh, J. Guo and A. Javey, *Acs Nano*, 2015, **9**, 2071–2079.

26 T. Roy, M. Tosun, J. S. Kang, A. B. Sachid, S. B. Desai, M. Hettick, C. C. Hu and A. Javey, *ACS Nano*, 2014, **8**, 6259–6264.

27 R. Cheng, D. Li, H. Zhou, C. Wang, A. Yin, S. Jiang, Y. Liu, Y. Chen, Y. Huang and X. Duan, *Nano Lett.*, 2014, **14**, 5590–5597.

28 M. M. Furchi, A. Pospischil, F. Libisch, J. Burgdorfer and T. Mueller, *Nano Lett.*, 2014, **14**, 4785–4791.

29 C. H. Lee, G. H. Lee, A. M. van der Zande, W. Chen, Y. Li, M. Han, X. Cui, G. Arefe, C. Nuckolls, T. F. Heinz, J. Guo, J. Hone and P. Kim, *Nat. Nanotechnol.*, 2014, **9**, 676–681.

30 P. Rivera, J. R. Schaibley, A. M. Jones, J. S. Ross, S. Wu, G. Aivazian, P. Klement, K. Seyler, G. Clark, N. J. Ghimire, J. Yan, D. G. Mandrus, W. Yao and X. Xu, *Nat. Commun.*, 2015, **6**, 6242.

31 W. T. Hsu, Z. A. Zhao, L. J. Li, C. H. Chen, M. H. Chiu, P. S. Chang, Y. C. Chou and W. H. Chang, *ACS Nano*, 2014, **8**, 2951–2958.

32 J. Kang, S. Tongay, J. Zhou, J. B. Li and J. Q. Wu, *Appl. Phys. Lett.*, 2013, **102**, 012111.

33 C. Gong, H. J. Zhang, W. H. Wang, L. Colombo, R. M. Wallace and K. J. Cho, *Appl. Phys. Lett.*, 2013, **103**, 053513.

34 N. Peimyoo, J. Z. Shang, C. X. Cong, X. N. Shen, X. Y. Wu, E. K. L. Yeow and T. Yu, *ACS Nano*, 2013, **7**, 10985–10994.

35 W. J. Zhao, Z. Ghorannevis, L. Q. Chu, M. L. Toh, C. Kloc, P. H. Tan and G. Eda, *ACS Nano*, 2013, **7**, 791–797.

36 B. Zhu, H. Zeng, J. Dai, Z. Gong and X. Cui, *Proc. Nat. Acad. Sci. USA*, 2014, **111**, 11606–11611.

37 Z. Ye, T. Cao, K. O'Brien, H. Zhu, X. Yin, Y. Wang, S. G. Louie and X. Zhang, *Nature*, 2014, **513**, 214–218.

38 H. R. Gutierrez, N. Perea-Lopez, A. L. Elias, A. Berkdemir, B. Wang, R. Lv, F. Lopez-Urias, V. H. Crespi, H. Terrones and M. Terrones, *Nano Lett.*, 2013, **13**, 3447.

39 J. S. Ross, S. Wu, H. Yu, N. J. Ghimire, A. M. Jones, G. Aivazian, J. Yan, D. G. Mandrus, D. Xiao, W. Yao and X. Xu, *Nat. Commun.*, 2013, **4**, 1474.

40 N. Kumar, Q. Cui, F. Ceballos, D. He, Y. Wang and H. Zhao, *Phys. Rev. B*, 2014, **89**, 125427.

41 S. Tongay, J. Zhou, C. Ataca, K. Lo, T. S. Matthews, J. B. Li, J. C. Grossman and J. Q. Wu, *Nano Lett.*, 2012, **12**, 5576–5580.

42 M. Z. Bellus, F. Ceballos, H.-Y. Chiu and H. Zhao, *ACS Nano*, 2015, **9**, 6459–6464.

43 L. M. Smith, D. R. Wake, J. P. Wolfe, D. Levi, M. V. Klein, J. Klem, T. Henderson and H. Morkoç, *Phys. Rev. B*, 1988, **38**, 5788–5791.

44 Q. Cui, F. Ceballos, N. Kumar and H. Zhao, *ACS Nano*, 2014, **8**, 2970–2976.

45 R. Wang, B. A. Ruzicka, N. Kumar, M. Z. Bellus, H.-Y. Chiu and H. Zhao, *Phys. Rev. B*, 2012, **86**, 045406.